Correlated electrons in the flat band in the charge density wave state of $4H_b-TaSe_xS_{2-x}$

Yanyan Geng,[1,2,*] Jianfeng Guo,[1,2,3,*] Fanyu Meng,[1,2,*] Manyu Wang,[1,2] Shuo Mi,[1,2] Li Huang,[3] Rui Xu,[1,2] Fei Pang,[1,2] Kai Liu,[1,2] Shancai Wang,[1,2] Hong-Jun Gao,[3] Weichang Zhou,[4] Wei Ji,[1,2,†] Hechang Lei,[1,2,‡] and Zhihai Cheng[1,2,§]

[1]*Key Laboratory of Quantum State Construction and Manipulation (Ministry of Education), Renmin University of China, Beijing 100872, China*

[2]*Beijing Key Laboratory of Optoelectronic Functional Materials & Micro-nano Devices, Department of Physics, Renmin University of China, Beijing 100872, China*

[3]*Beijing National Laboratory for Condensed Matter Physics, Institute of Physics, Chinese Academy of Sciences, Beijing 100190, China*

[4]*Key Laboratory of Low-dimensional Quantum Structures and Quantum Control of Ministry of Education, School of Physics and Electronics, Institute of Interdisciplinary Studies, Hunan Normal University, Changsha 410081, China*

(Received 12 June 2024; revised 8 August 2024; accepted 19 August 2024; published 5 September 2024)

Many intriguing quantum states of matter, such as unconventional superconductivity, magnetic phases, and fractional quantum Hall physics, emerge from the spatially correlated localized electrons in the flat bands of solid materials. By using scanning tunneling microscopy and spectroscopy (STM/STS), we report on the real-space investigation of correlated electrons in the flat band of superlattice $4H_b$-$TaSe_xS_{2-x}$. In contrast with the pristine $4H_b$-TaS_2, the selenium (Se) substitutions significantly affect the interfacial transfer of correlated electrons between the charge density wave (CDW) states of 1*T*- and 1*H*-TaS_2 layers and contribute the real-space fractional electron-filling configurations with the distributed electron-filled and void Star of David (SoD) clusters of the 1*T* layer. The site-specific STS spectra directly reveal their respective prominent spectra weight above E_F and symmetric Mott-like spectra. In addition, the spatial distributions of these electron-filled SoDs in the 1*T* layer of $4H_b$-$TaSe_{0.7}S_{1.3}$ demonstrate different local short-range order, clearly indicating the complex neighboring interactions among the localized electrons in the flat band of the 1*T* layer. Our results not only provide in-depth insight into correlated electrons in the flat CDW band but also provide a simple platform to manipulate the electron-correlation-related quantum states.

DOI: 10.1103/PhysRevB.110.115107

I. INTRODUCTION

Flat bands, characterized by their high density of states, dispersionless nature, and strong correlation, have gained considerable attention from both condensed matter physics and materials science. As a special electron band structure, the flat band has many energy-degenerate electrons, which can still be confined in real space in lattices supporting dispersionless electronic excitation in momentum space. Owing to the dominance of electron-electron interactions over the quenched kinetic energy, materials hosting electronic flat bands serve as a promising venue for exploring various exotic phenomena, including unconventional superconductivity [1–3], magnetic phases [4,5], fractional quantum Hall physics [6], excitonic insulating behavior [7,8], and charge density wave (CDW) states [9–11]. Recent advances in kagome lattices [12,13], twisted bilayer graphene, and twisted transition metal dichalcogenides (TMDs) in moiré superlattice systems [9,14], as well as in some TMDs with CDWs [15,16], have spurred researchers to explore the realization of flat bands in a broader range of material systems.

TaS_2 is one of the most studied CDW materials with rich crystal structures and physical properties [17,18]. The 1*T*-TaS_2 manifests a strong-correlation Mott-insulating ground state in the commensurate CDW (CCDW) state [19]. In the CCDW state, every 13 Ta atoms shrink into a cluster named the Star of David (SoD). Subsequently, these SoD clusters arrange into an ordered triangular $\sqrt{13}\times\sqrt{13}$ superlattice, as depicted in Fig. 1(a). Each SoD is composed of 13 Ta 5*d* electrons, with the 12 electrons of the peripheral Ta atoms pairing to form six fully occupied insulating bands and leaving a single unpaired electron (Mott) of the central Ta atom in a half-filled metallic band at E_F. This half-filled band subsequently splits into upper and lower Hubbard bands (UHB and LHB) due to the significant on-site Coulomb interaction (*U*), thereby giving rise to a Mott insulator. However, authors of recent studies have demonstrated that the interlayer CDW dimerization results in the formation of a band insulator rather than a correlated one [20–22]. In contrast, 2*H*-TaS_2 exhibits metallic behavior, coexisting with a commensurate 3×3 CDW at ~78 K [Fig. 1(b)] and exhibits superconductivity at ~0.8 K [23]. The typical STM images of the $\sqrt{13}\times\sqrt{13}$ CDW (1*T* layer) and 3×3 CDW (2*H* layer) are presented in Figs. 1(c) and 1(d), respectively.

*These authors contributed equally to this work.
†Contact author: wji@ruc.edu.cn
‡Contact author: hlei@ruc.edu.cn
§Contact author: zhihaicheng@ruc.edu.cn

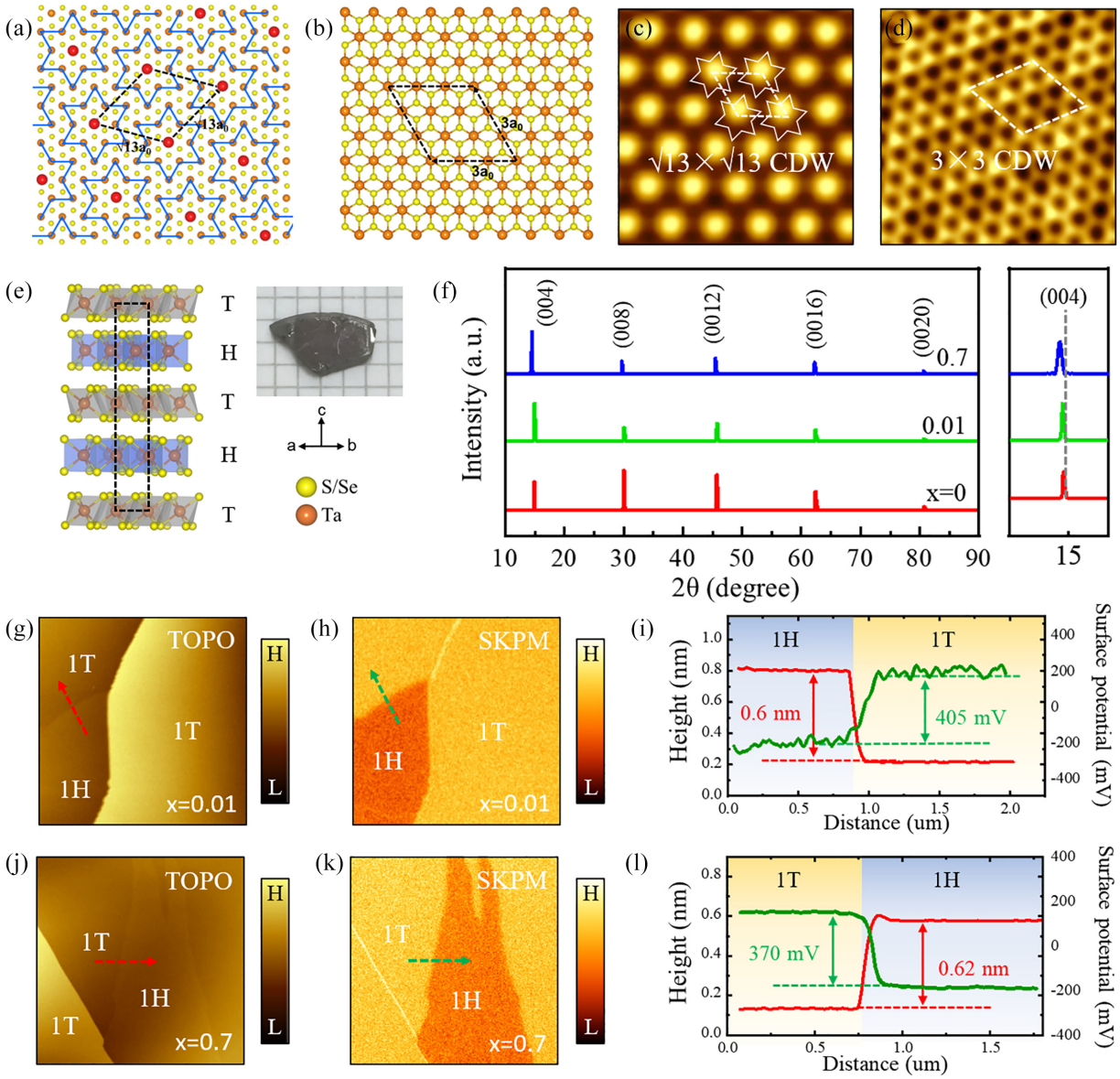

FIG. 1. Crystal structure and scanning Kelvin probe force microscopy (SKPM) characterization of superlattice $4H_b$-$TaSe_xS_{2-x}$. Schematic illustrations of the (a) 1*T* layer and (b) 2*H* layer. The supercells of the $\sqrt{13} \times \sqrt{13}$ charge density wave (CDW; 1*T* layer) and 3×3 CDW (2*H* layer) are marked by the black dashed lines in (a) and (b), respectively. The Star of David (SoD) clusters of the $\sqrt{13} \times \sqrt{13}$ CDW state in 1*T* layer are outlined by the blue stars with the central localized electrons of CDW flat band. Typical scanning tunneling microscopy (STM) images of (c) 1*T*-TaS_2 and (d) 2*H*-TaS_2. The $\sqrt{13} \times \sqrt{13}$ CDW (1*T* layer) and 3×3 CDW (2*H* layer) are clearly visible. (e) Crystal structure and typical optical image of the $4H_b$-$TaSe_xS_{2-x}$ single crystal. The Ta and S/Se atoms are shown in orange and yellow, respectively. (f) X-ray diffraction (XRD) patterns of $4H_b$-TaS_2, $4H_b$-$TaSe_{0.01}S_{1.99}$, and $4H_b$-$TaSe_{0.7}S_{1.3}$. (g) Atomic force microscopy (AFM) topography and (h) SKPM surface potential images of $4H_b$-$TaSe_{0.01}S_{1.99}$. (i) Line profile along the dashed line in (g) and (h). The step height and surface potential difference between the 1*T* and 1*H* layers are ~0.6 nm and ~400 mV, respectively. (j) AFM topography and (k) SKPM surface potential images of $4H_b$-$TaSe_{0.7}S_{1.3}$. (l) Line profile along the dashed line in (j) and (k). The step height and surface potential difference between the 1*T* and 1*H* layers are ~0.62 nm and ~370 mV, respectively. Imaging parameters: (a) $6 \times 6\,nm^2$; (b) $3 \times 3\,nm^2$; (f), (g), (i), and (j) $5 \times 5\,\mu m^2$.

Utilizing the van der Waals nature of TaS_2, it can be spontaneously integrated into a superlattice comprising alternating insulating *T*- and metallic *H*-phase layers, which are recognized as the $4H_b$ phase [Fig. 1(e)] and 6*R* phase [24,25]. $4H_b$-TaS_2 has evoked great interest owing to the ability to induce new electronic ground states not present in the *T* or *H* phases, which profoundly alter its superconducting and Mott ground states. Authors of recent studies have revealed the existence of the chiral superconducting phase [26], two-component nematic superconductivity [27], and topological nodal superconductivity of the 1*H* layer [28]. Scanning tunneling spectroscopy (STS) measurements reported the narrow electronic bands above E_F of the 1*T* layer of $4H_b$-TaS_2 [29] and the Kondo effect on $1T/1H$ bilayers grown by molecular beam epitaxy [30] or some specific CDW sites of the 1*T* layer of $4H_b$-TaS_2 [31]. In addition to their intrinsic states, more exotic states can be induced by an electric field [31], temperature [32], substrate [33], and so on. Precise

isovalent Se substitution is also an effective method, which does not introduce extra electrons or holes into the system. The study of temperature-dependent resistivity showed that the superconducting transition temperature is highest (∼4.1 K) and the 3×3 CDW of the $1H$ layer at ∼22 K at the optimal Se substitution content of 0.7 [34]. Significantly, Se substitution can also alter the interlayer distance [32], which effectively modifies the interlayer charge transfer of electrons [35]. Authors of most studies have focused on the effect of Se substitution on superconductivity and transport properties of $4H_b$-TaS_2 [32,34]; however, few authors have concentrated on the changes in electronic structure induced by Se substitution in real space.

In this paper, the real-space investigation of correlated electrons in the flat band of superlattice $4H_b$-$TaSe_xS_{2-x}$ is reported by STM/STS. Compared with the pristine $4H_b$-TaS_2, the effects of Se substitution on the work function (surface potential) difference, CDW order, interfacial transfer of correlated electron, electron-filling factors of the flat band, and spatial fractional electron-filling configurations with the distributed electron-filled and void SoD clusters of the $1T$ layer are given in detail. Site-specific STS spectra reveal the symmetric Mott-like spectra and prominent spectra weight above E_F of electron-filled and void SoD clusters of the $1T$ layer, respectively. Furthermore, we identify distinct local short-range patterns of these electron-filled SoDs in the $1T$ layer of $4H_b$-$TaSe_{0.7}S_{1.3}$, which can be ascribed to the intricate interplay of neighboring interactions among the localized electrons in the flat band of the $1T$ layer.

II. RESULTS AND DISCUSSION

Figure 1(f) illustrates the impact of Se substitution on the layer spacing of $4H_b$-$TaSe_xS_{2-x}$ single crystals. The x-ray diffraction (XRD) patterns of $4H_b$-TaS_2, $4H_b$-$TaSe_{0.01}S_{1.99}$, and $4H_b$-$TaSe_{0.7}S_{1.3}$ single crystals are displayed in Fig. 1(f), where only (00l) reflections are observed, indicating that the c axis is perpendicular to the surface of the crystal. With increasing Se, the diffraction peaks distinctly shift to lower angles, signifying crystal expansion due to Se substitution. This observation confirms that the Se substitution in $4H_b$-TaS_2 effectively increases the interlayer spacing. Additional atomic force microscope (AFM) topography and scanning Kelvin probe force microscopy (SKPM) surface potential images of $4H_b$-TaS_2, $4H_b$-$TaSe_{0.01}S_{1.99}$, and $4H_b$-$TaSe_{0.7}S_{1.3}$ are presented in Fig. S2 in the Supplemental Material [36] (see also Refs. [37,38] therein) and Figs. 1(g)–1(l), respectively.

Owing to their distinct electronic properties, the $1T$ ($1H$) layers can be readily distinguished by the relatively high (low) surface potentials in the SKPM images. The surface potential difference between the $1T$ and $1H$ layers is ∼400 mV for both $4H_b$-TaS_2 and $4H_b$-$TaSe_{0.01}S_{1.99}$ (Figs. 1(i) and S2(c) in the Supplemental Material [36]). This finding agrees with previous studies, in which authors have reported that the work function of the $1H$ layer is ∼5.6 eV, whereas that of the $1T$ layer is ∼5.2 eV [37]. With increasing Se, a significant reduction in E_F of the $1T$ layers is induced [38], which corresponds to the decreased surface potential difference (∼370 mV) observed in $4H_b$-$TaSe_{0.7}S_{1.3}$, as shown in Figs. 1(l) and S2 in the Supplemental Material [36] (see also Refs. [37,38] therein). The increased interlayer distance and reduced surface potential difference make $4H_b$-$TaSe_{0.7}S_{1.3}$ an exemplary platform for investigating interfacial charge transfer of electrons and spatial distributions of correlated electrons in the flat CDW band of the $1T$ layer.

A series of detailed STM images and corresponding fast Fourier transform (FFT) patterns of $4H_b$-$TaSe_{0.01}S_{1.99}$ and $4H_b$-$TaSe_{0.7}S_{1.3}$ are presented in Figs. 2(a)–2(d). The CDW of the $1T$ layer of $4H_b$-$TaSe_{0.01}S_{1.99}$ and $4H_b$-$TaSe_{0.7}S_{1.3}$ maintains the $\sqrt{13} \times \sqrt{13}$ SoD patterns as that in the intrinsic $4H_b$-TaS_2 sample [29] at positive bias [Figs. 2(a) and 2(c)]. However, for the $1H$ layer in $4H_b$-$TaSe_xS_{2-x}$, the 3×3 CDW is gradually suppressed with the increase of Se concentration [39]. For $4H_b$-$TaSe_{0.01}S_{1.99}$, the 3×3 CDW of the $1H$ layer is suppressed to 1×3 CDW [Fig. 2(b)], whereas the 3×3 CDW of the $1H$ layer is negligible of $4H_b$-$TaSe_{0.7}S_{1.3}$, displaying 1×1 periodicity (Figs. 2(d) and S3 in the Supplemental Material [36]).

How does Se substitution modify the CCDW order of the $1T$ layer? Figures 2(e)–2(g) display the large-scale STM images and corresponding FFT patterns of the $1T$ layer of $4H_b$-$TaSe_{0.01}S_{1.99}$ and $4H_b$-$TaSe_{0.7}S_{1.3}$. Unlike the pristine $4H_b$-TaS_2 sample, an insignificant amount of Se substitution induces the formation of several CCDW phase domain walls within the $1T$ layer, as depicted in Figs. 2(e) and S10 in the Supplemental Material [36]. As the Se concentration is increased from 0.01 to 0.7, the number of domain walls proliferates, and the $1T$ surface fragments into domains with varying sizes and distinct boundaries, like the so-called *mosaic* phase in $1T$-TaS_2 induced by a voltage pulse [40]. In addition, the large chiral CDW domains emerge within the mosaiclike CDW states, with the R- and L-chiral domains separated by white chiral domain walls (Figs. 2(f)–2(g) and S11 in the Supplemental Material [36]). Intriguingly, under negative bias, two distinguished brightnesses of SoDs, one bright and one dark, can be clearly observed of $4H_b$-$TaSe_{0.7}S_{1.3}$ [Figs. 2(g) and 2(h)], while for $4H_b$-$TaSe_{0.01}S_{1.99}$, a few dispersed bright SoDs emerge (Fig. S4 in the Supplemental Material [36]). A similar effect of Se substitution on the CCDW was observed in the STM images of $1T$-TaS_2, as reported in the work of Qiao *et al* [41]. Through a meticulous comparison of the impact of Se substitution on the CCDW of $1T$-TaS_2, we conclude that this brightness appearance is not topographic but may derive from different electron fillings of SoDs rather than just the effect of chemical disorder from quenched Se/S [41]. This characteristic is more analogous to the bright-dark distribution of SoDs on the hole Ti-doped $1T$-TaS_2 surface [42].

To elucidate the origin of these bright and dark SoDs of the $1T$ layer, different stacking orders, including $1T/1T$, $1T/1H$, and $1H/1T$ of $4H_b$-$TaSe_{0.7}S_{1.3}$ are investigated in Figs. 2(i)–2(l). Notably, the $1T/1H$ and $1T/1T$ stacking regions are distinctly identifiable at the negative bias (occupied state), while at positive bias (unoccupied state), all SoDs in both $1T/1T$ and $1T/1H$ regions exhibit the same shape and brightness [Figs. 2(i) and 2(j)]. In contrast with the homogeneously distributed SoDs of the $1T/1T$ region, the number of bright SoDs of the $1T/1H$ region is significantly reduced, displaying a pattern of alternating bright and dark SoDs at occupied states. These observations illustrate that the charge transfer

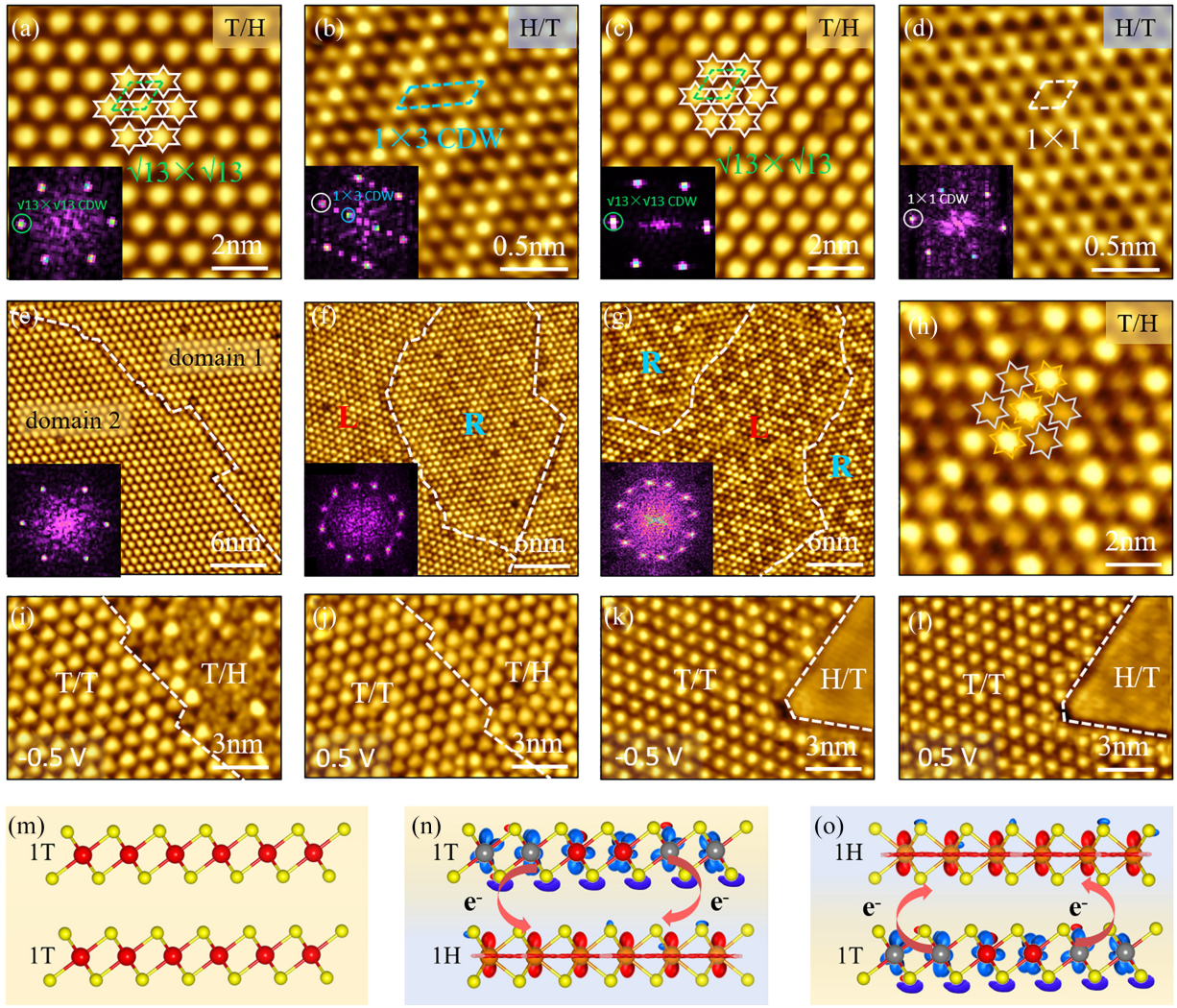

FIG. 2. Scanning tunneling microscopy (STM) measurements of $4H_b$-$TaSe_{0.01}S_{1.99}$ and $4H_b$-$TaSe_{0.7}S_{1.3}$. STM images and corresponding fast Fourier transform (FFT) patterns of (a) and (c) the $1T$ layer and (b) and (d) the $1H$ layer of $4H_b$-$TaSe_{0.01}S_{1.99}$ and $4H_b$-$TaSe_{0.7}S_{1.3}$. The commensurate $\sqrt{13} \times \sqrt{13}$ charge density wave (CDW) of the $1T$ layer are preserved in both (a) and (c), while the 3×3 CDW of the $1H$ layer are suppressed to 1×3 CDW ($4H_b$-$TaSe_{0.01}S_{1.99}$) and negligible CDW ($4H_b$-$TaSe_{0.7}S_{1.3}$), respectively. (e) STM image and corresponding FFT pattern of the $1T$ layer in $4H_b$-$TaSe_{0.01}S_{1.99}$, with a small number of phase domains observed. Image was recorded under tunneling condition $V_b = 500$ mV, $I_t = 100$ pA. Large-scale STM images and corresponding FFT patterns of the $1T$ layer of $4H_b$-$TaSe_{0.7}S_{1.3}$ taken with (f) positive and (g) negative bias. Both CDW phase and chiral domain walls are observed. Imaging parameters: (f) $V_b = 0.6$ V, $I_t = 100$ pA; (g) $V_b = -0.6$ V, $I_t = 100$ pA. (h) A zoom-in STM image from (g), showing the distributed bright Star of David (SoD; orange stars) and dark SoD clusters (gray stars). STM images of $1T/1T$, $1T/1H$, and $1H/1T$ stacking regions in $4H_b$-$TaSe_{0.7}S_{1.3}$ taken with (i) and (k) positive and (j) and (l) negative bias. The charge transfer at the $1T/1H$ heterointerface contributes the apparent difference of the $1T$ layer at occupied and unoccupied states. Imaging parameters: (i) and (k) $V_b = 500$ mV, $I_t = 100$ pA; (j) and (l) $V_b = -500$ mV, $I_t = 100$ pA. (m)–(o) Schematic model of interlayer charge transfer of $1T/1T$, $1T/1H$, and $1H/1T$ stacking order. Blue and red represent the electron depletion and accumulation regions.

at the $1T/1H$ heterointerface contributes to the apparent difference of the $1T$ layer at occupied and unoccupied states. This can be further demonstrated by STM images of $1T/1T$ and $1H/1T$ stacking regions in $4H_b$-$TaSe_{0.7}S_{1.3}$ taken under positive and negative bias in Figs. 2(k) and 2(l). Figures 2(m)–2(o) present a schematic model of interlayer charge transfer for the $1T/1T$, $1T/1H$, and $1H/1T$ stacking orders, where the $1H$ layer serves as a charge reservoir, taking away electrons from the $1T$ layer. However, compared with the $1T/1H$ overall electron distribution of intrinsic $4H_b$-TaS_2, the $1T/1H$ order of $4H_b$-$TaSe_{0.7}S_{1.3}$ demonstrates a spatial localized electron-filled configuration with the bright and dark SoD distribution. We attribute this discrepancy to selenium substitution, which effectively alters the interlayer charge transfer mechanism of electrons from a complete to a partial charge transfer (Fig. S5 in the Supplemental Material [36], see also Ref. [31] therein).

Next, we turn to site-specific STS spectra measurements on the $1T$ layer of $4H_b$-$TaSe_{0.01}S_{1.99}$ and $4H_b$-$TaSe_{0.7}S_{1.3}$ to examine the origin of the bright and dark SoDs, as shown in Fig. 3. Compared with the pristine $4H_b$-TaS_2 sample, a few bright triangular SoDs emerge in the $1T$ layer of

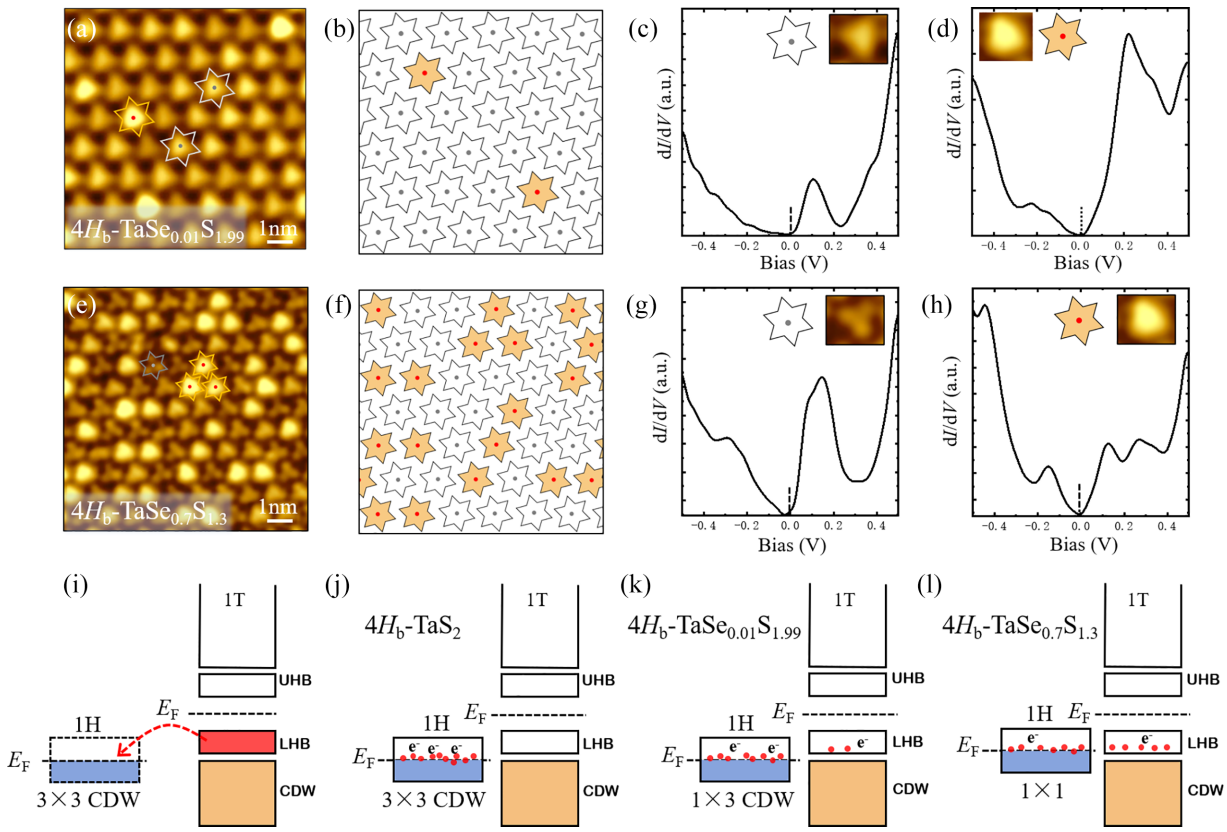

FIG. 3. Electronic states of the 1T layer of $4H_b$-$TaSe_{0.01}S_{1.99}$ and $4H_b$-$TaSe_{0.7}S_{1.3}$. (a) Typical scanning tunneling microscopy (STM) image and (b) schematic model of the distributed Stars of David (SoDs) in the 1T layer of $4H_b$-$TaSe_{0.01}S_{0.7}$. The central electron-filled and void SoDs are marked by the stars with the central red and gray dots, respectively. Typical dI/dV spectra of (c) dark and (d) bright SoDs in (a) and (b). (e) Typical STM image and (f) schematic model of the distributed SoDs in the 1T layer of $4H_b$-$TaSe_{0.7}S_{1.3}$. Typical dI/dV spectra of (g) dark and (h) bright SoDs in (e) and (f). Different from the intrinsic Mott spectra in 1T-TaS_2, the dI/dV spectra of electron-filled and void SoDs show prominent spectra weight above E_F and symmetric Mott-like spectra weight with small U, respectively. (i)–(l) Schematic of band diagrams for the interfacial electron transfer in 1T-TaS_2, $4H_b$-TaS_2, $4H_b$-$TaSe_{0.01}S_{1.99}$, and $4H_b$-$TaSe_{0.7}S_{1.3}$. Imaging parameters: (a) $V_b = -1$ V, $I_t = 100$ pA; (c) and (e) $V_b = -500$ mV, $I_t = 100$ pA.

$4H_b$-$TaSe_{0.01}S_{1.99}$, as shown in Figs. 3(a) and 3(b). The bright triangular SoDs exhibit a Mott-like V-shaped gap (Figs. 3(d) and S6 in the Supplemental Material [36]), while the dark triangular SoDs display an electron-hole asymmetric single pronounced peak above E_F [Fig. 3(c)], in almost coincidence with the dI/dV spectra of the 1T layer of typical $4H_b$-TaS_2 [29]. The coexistence of these two distinct spectra of bright and dark triangular SoDs of $4H_b$-$TaSe_{0.01}S_{1.9}$ has not been previously reported in $4H_b$-TaS_2. The difference of bright and dark SoDs reflects the different electron fillings of the SoDs of the 1T layer, where bright and dark SoDs represent the electron-filled and void SoDs, respectively. The Se substitution causes the emergence of very few electrons in the flat band, which appear as bright SoDs (electron-filled) in real space, while most of the dark SoDs (electron-void) are essentially indistinguishable from the intrinsic $4H_b$-TaS_2.

Typical STM images and schematic diagrams of the 1T layer of $4H_b$-$TaSe_{0.7}S_{1.3}$ are given in Figs. 3(e) and 3(f), illustrating an alternating pattern of bright triangular and dark three-petal-flower SoDs. The corresponding dI/dV spectra of the dark three-petal flower and the bright triangle SoDs of $4H_b$-$TaSe_{0.7}S_{1.3}$ are shown in Figs. 3(g) and 3(h), respectively. The dI/dV spectra of dark three-petal-flower SoDs featured by spectral weight transfer prominent spectra weight above E_F with suppression of the LHB, like the dI/dV spectra of dark triangular SoDs of $4H_b$-$TaSe_{0.01}S_{1.99}$, while the STS of the bright triangular SoDs shows symmetric Mott-like spectra weight with small U compared with $4H_b$-$TaSe_{0.01}S_{1.99}$. The small gap size of $4H_b$-$TaSe_{0.7}S_{1.3}$ could be due to the modification of the bandwidth and/or the screening of the Coulomb interaction by the influence of the 1×3 CDW/1×1 of the metallic 1H layer. These diverse electronic states emerging from different SoD configurations indicate the band filling as a pivotal factor in the complexity of $4H_b$-$TaSe_{0.01}S_{1.99}$ and $4H_b$-$TaSe_{0.7}S_{1.3}$.

Schematic of band diagrams for the interfacial electron transfer in $4H_b$-TaS_2, $4H_b$-$TaSe_{0.01}S_{1.99}$, and $4H_b$-$TaSe_{0.7}S_{1.3}$ are illustrated in Figs. 3(i)–3(l). For the intrinsic $4H_b$-TaS_2, the work function difference between the 1T and 1H layers results in a substantial interface charge transfer, leading to the heavily hole-doped 1T layer, where 1e per SoD is transferred from the 1T to the 1H layer [33,35]. Interface charge transfer contributes to the overall empty state ($n = 0$) and depleted flat

band above E_F of the $1T$ layer in $4H_b$-TaS_2 [Fig. 3(j)]. In line with this, the $1T$ layer of $4H_b$-TaS_2 shows a hole-doped Mott state with the spectral peak formed just above E_F.

With the substitution of Se, the interlayer distance increases, inducing a decrease in interlayer hybridization and interlayer charge transfer (Fig. S7 in the Supplemental Material [36], see also Ref. [35] therein), where the flat band of the $1T$ layer changes from completely empty to partially occupied. For $4H_b$-$TaSe_{0.01}S_{1.99}$, the Se substitution causes the emergence of very few electrons in the flat band, which appear as bright SoDs (electron-filled) in real space [Fig. 3(k)]. When the Se substitution concentration is 0.7, the charge transfer decreases from 1e to 0.7e [35], and the flat band filling factor increases accordingly from 0 to 0.3e [Fig. 3(l)], which is consistent with the results of the partially filled flat bands of angle-resolved photoemission spectroscopy [43]. Once the flat band starts to host a portion of the electron, the peak of the flat band shifts toward E_F, and a considerably small Coulomb interaction U would be sufficient to cause a band splitting (Fig. S8 in the Supplemental Material [36], see also Ref. [35] therein). The partially filled flat bands contribute the spatial electron-filling configurations with the distributed electron-filled and void SoD clusters of the $1T$ layer.

In addition, another factor affecting the size of the charge transfer and the real-space electron distribution of the $1T$ layer may be the presence or absence of a 3×3 CDW of the $1H$ layer. We suggest that the 1×1 has a higher work function than the 3×3 CDW of the $1H$ layer, so fewer electrons are transferred from the $1T$ layer, and that the 1×1 is more metallic, providing stronger Coulomb screening of the $1T$ layer. These observations imply that interlayer charge transfer can be modulated by the Se substitution and CDW substrate of the $1H$ layer, and the band filling is crucial to determining the spatial electron-filling configurations of the $1T$ layer.

The spatial distribution of the bright (electron-filled) SoDs of the $1T$ layer in $4H_b$-$TaSe_{0.7}S_{1.3}$ was further investigated by a large number of STM images, as shown in Figs. 4(a) and S9 in the Supplemental Material [36]. The apparent height of bright (electron-filled) and dark (electron-void) SoDs is different in the occupied state [Fig. 4(b)]. Based on these differences, we can estimate the overall electron-filling factor in the $1T$ layer to be $n = \frac{1}{3}$ [Fig. 4(c)], which reflects the interlayer electron transfer. Contrary to the overall uniform electron transfer observed in $4H_b$-TaS_2, $4H_b$-$TaSe_{0.7}S_{1.3}$ demonstrates spatially localized electron transfer. A meticulous examination reveals that the spatial distribution of the bright SoDs is not arbitrary but displays certain correlated order, such as stripelike, short-range 1×2 SoDs and anti-seven magic number electron configurations [Figs. 4(e)–4(g)], which reflect the complex neighboring interactions among the electrons in the $1T$ layer. To elucidate the nearest-neighbor interactions among the bright SoDs, the assembled form of the nearest-neighbor SoDs was quantified [Fig. 4(d)]. The histogram of nearest-neighbor SoD configurations indicates that bright SoDs tend to cluster in a $\frac{4}{5}-$SoD arrangement rather than preferring to exist in isolation or to form a 7-SoD configuration. The stripelike SoDs and SoD clusters suggest the presence of nearest-neighbor attractive interactions among bright SoDs, while the short-range 1×2 SoDs and anti-seven magic number (7-SoD) electron configurations imply the existence of configuration-dependent repulsive interactions.

Authors of previous studies using STM and scanning microwave impedance microscopy (SMIM) techniques have confirmed the existence of a generalized Wigner crystal state with different fractional fillings in the twisted system, which can be described by a simple Coulomb gas model [1,45,46]. The ordered patterns of Monte Carlo (MC) simulations based on the Coulomb gas model with different fractional fillings are shown in Figs. 4(h)–4(k). Compared with the ordered patterns of MC simulations, our electron distributions demonstrate some different patterns at the same fractional filling such as SoD clusters and short-range order. This difference derives from the fact that only the long-range Coulomb repulsion is considered in the Coulomb gas model, whereas the aggregated behavior of the electrons and the local ordering structure of $4H_b$-$TaSe_{0.7}S_{1.3}$ may originate from the short-range attractive interactions between the electrons. The origin of the attractive interactions is not clear and needs to be further investigated in combination with theoretical calculations.

III. CONCLUSIONS

$4H_b$-TaS_2 interleaves the Mott-insulating state of $1T$-TaS_2 and the putative spin liquid it hosts together with the metallic state of $2H$-TaS_2 and the low-temperature superconducting phase it harbors, providing a good platform for the investigation of the competition/cooperation between superconductivity and CDW order. Authors of recent studies have illustrated the difference in spectroscopic between the Kondo resonated $1T/1H$ bilayer and the hole-doped Mott insulator $4H_b$-TaS_2, implying that doping levels in the Mott-insulating $1T$ layer can be effectively modulated through the interlayer coupling. Regarding the tuning means for the interlayer coupling, the isovalent Se substitution acts as an effective method, which effectively modify the interlayer distance.

We investigated the effect of the Se substitution on the work function, CDW order, the interfacial electrons transfer between the $1T$ and $1H$ layers, and the electron-filled of flat band of the $1T$ layer of superlattice $4H_b$-$TaSe_xS_{2-x}$ in detail. Significantly, compared with pristine $4H_b$-TaS_2, Se substitution increases the interlayer distance between the $1T$ and $1H$ layers, accompanied by a decrease in charge transfer and interlayer hybridization. The decrease of charge transfer contributes spatial fractional electron-filling configurations with the distributed electron-filled and void SoD clusters of the $1T$ layer. STS spectra further exhibit respective prominent spectra weight above E_F and symmetric Mott-like spectra of electron-filled and void SoD clusters. In this paper, we provide insights into understanding correlated electrons of flat bands of the superlattice $4H_b$-$TaSe_xS_{2-x}$, but the effect on chiral superconductivity is not yet known. The influence of different substitution ratios on CDW and superconductivity can be explored at lower temperatures in the future to realize more exotic quantum states. Furthermore, the complex interactions between localized electrons of the $1T$ layer provide a simple platform to control the electron-correlation-related quantum states.

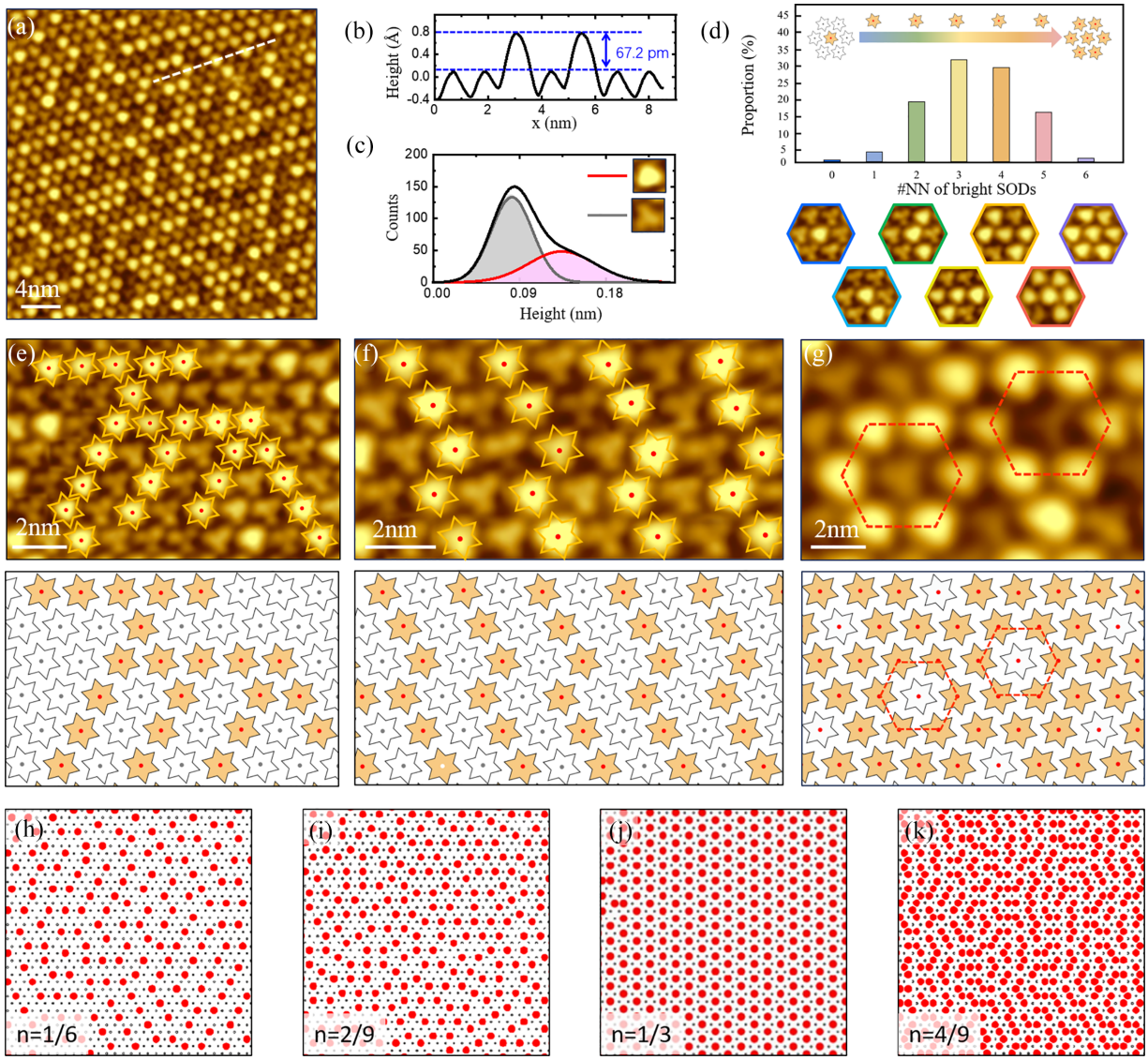

FIG. 4. Correlated electron distributions of the 1T layer of 4H_b-$TaSe_{0.7}S_{1.3}$. (a) Representative large-scale scanning tunneling microscopy (STM) image of electron distributions. (b) The height profile along the dashed line in (a) shows a height difference of ∼67.5 pm between the bright and dark Stars of David (SoDs). (c) Apparent height distribution curves of (a). The bright SoDs account for ∼30% of all SoDs in the 1T layer of 4H_b-$TaSe_{0.7}S_{1.3}$. (d) Histogram counting nearest-neighbor SoDs having different brightness, averaged over 15 STM images (∼7000 SoDs). The illustrations show the configuration types associated with the histogram values, taking the central SoDs of the seven-SoD plaquette as a reference. All other configurations can be derived by arrangement permutations. High-resolution STM images (top) and their schematic models (bottom) of (e) the observed striplike, (f) short-range 1 × 2 SoDs, and (g) anti-seven magic number electron configurations. Reproduced electrons patterns (marked by red dots) in the triangular lattice at fractional fillings of (h) $n = \frac{1}{6}$, (i) $n = \frac{2}{9}$, (j) $n = \frac{1}{3}$, and (k) $n = \frac{4}{9}$ simulated based on a Coulomb gas model [44]. Imaging parameters: (a) and (e)–(g) $V_b = -500$ mV, $I_t = 100$ pA.

IV. MATERIALS AND METHODS

The high-quality 4H_b-$TaSe_xS_{2-x}$ single-crystal samples were grown by the chemical vapor transport method with iodine as the transport agent. Stoichiometric amounts of high-purity elements Ta (99.9%), S (99.9%), and Se (99.95%) were mixed. The doping was uniformly and precisely controlled in high-quality samples. The 4H_b-$TaSe_xS_{2-x}$ crystals were cleaved at room temperature in ultrahigh vacuum at a base pressure of 2×10^{-10} Torr and directly transferred to the cryogen-free low-temperature STM system (PanScan Freedom-LT, RHK). Chemically etched Pt-Ir tips were used and calibrated on a clean Ag(111) for STM and STS measurements. All the STM/STS measurements were performed at the base temperature of ∼9 K. The differential conductance (dI/dV) spectra were measured in constant-height mode using standard lock-in techniques. Gwyddion was used for STM data analysis.

The authors declare that the data supporting the findings in this paper are available within this paper and its Supplemental Material [36].

ACKNOWLEDGMENTS

This project was supported by the National Key R&D Program of China (Grant No. 2023YFA1406500), the National Natural Science Foundation of China (Grants No. 21622304, No. 61674045, No. 11604063, No. 11974422, No. 12104504, No. 12374200, and No. 12174443), the Strategic Priority Research Program (Chinese Academy of Sciences; Grant No. XDB30000000), and the Fundamental Research Funds for the Central Universities and the Research Funds of Renmin University of China [Grants No. 21XNLG27 (Z.C.) and No. 22XNH095 (H.D.)]. H.L. is supported by the Beijing Natural Science Foundation (Grant No. Z200005), the National Key R&D Program of China (Grants No. 2022YFA1403800 and No. 2023YFA1406500), and the National Natural Science Foundation of China (Grant No. 12274459). Y.G. was supported by the Outstanding Innovative Talents Cultivation Funded Programs 2023 of Renmin University of China.

Y.G., M.W., and Z.C. performed the STM experiments and analysis of STM data. S.M., J.G., R.X., F.P., K.L., and S.W. helped in the experiments. F.M. and H.L. provided the sample. W.J. and Z.C. wrote the manuscript with inputs from all authors.

The authors declare no competing financial interests.

[1] M. Yankowitz, S. W. Che, H. Polshyn, Y. X. Zhang, K. Watanabe, T. Taniguchi, D. Graf, A. F. Young, and C. R. Dean, Tuning superconductivity in twisted bilayer graphene, Science **363**, 1059 (2019).

[2] X. B. Lu, P. Stepanov, W. Yang, M. Xie, M. A. Aamir, I. Das, C. Urgell, K. J. Watanabe, T. Taniguchi, G. Y. Zhang *et al.*, Superconductors, orbital magnets and correlated states in magic-angle bilayer graphene, Nature (London) **574**, 653 (2019).

[3] J. Y. Duan, D. S. Ma, R. W. Zhang, W. Jiang, Z. Y. Zhang, C. X. Cui, Z. M. Yu, and Y. G. Yao, Cataloging high-quality two-dimensional van der Waals materials with flat bands, Adv. Funct. Mater. **34**, 2313067 (2024).

[4] A. L. Sharpe, E. J. Fox, A. W. Barnar, J. Finney, K. J. Watanabe, T. Taniguch, and M. A. Kastner, Emergent ferromagnetism near three-quarters filling in twisted bilayer graphene, Science **365**, 605 (2019).

[5] M. Ochi, M. Koshino, and K. Kuroki, Possible correlated insulating states in magic-angle twisted bilayer graphene under strongly competing interactions, Phys. Rev. B **98**, 081102(R) (2018).

[6] D. C. Tsui, H. L. Stormer, and A. C. Gossard, Two-dimensional magnetotransport in the extreme quantum limit, Phys. Rev. Lett. **48**, 1559 (1982).

[7] Y. Cao, V. Fatemi, A. Demir, S. Fang, S. L. Tomarken, J. Y. Luo, J. D. Sanchez-Yamagishi, K. Watanabe, T. Taniguchi, E. Kaxiras *et al.*, Correlated insulator behaviour at half-filling in magic-angle graphene superlattices, Nature (London) **556**, 80 (2018).

[8] Y. Cao, V. Fatemi, S. Fang, K. Watanabe, T. Taniguchi, E. Kaxiras, and P. Jarillo-Herrero, Unconventional superconductivity in magic-angle graphene superlattices, Nature (London) **556**, 43 (2018).

[9] J. M. Carpinelli, H. H. Weitering, E. W. Plummer, and R. Stumpf, Direct observation of a surface charge density wave, Nature (London) **381**, 398 (1996).

[10] M. Calandra, Phonon-assisted magnetic mott-insulating state in the charge density wave phase of single-layer $1T$-$NbSe_2$, Phys. Rev. Lett. **121**, 026401 (2018).

[11] W. Wang, B. Wang, Z. Gao, G. Tang, W. Lei, X. Zheng, H. Li, X. Ming, and C. Autieri, Charge density wave instability and pressure-induced superconductivity in bulk $1T$-$NbSe_2$, Phys. Rev. B **102**, 155115 (2020).

[12] N. J. Ghimire and I. I. Mazin, Topology and correlations on the kagome lattice, Nat. Mater. **19**, 137 (2020).

[13] M. Han, H. Inoue, S. Fang, C. John, L. Ye, M. K. Chan, D. Graf, T. Suzuki, M. P. Ghimire, W. J. Cho *et al.*, Evidence of two-dimensional flat band at the surface of antiferromagnetic kagome metal FeSn, Nat. Commun. **12**, 5345 (2021).

[14] D. Pei, B. Wang, Z. Zhou, Z. He, L. An, S. He, C. Chen, Y. Li, L. Wei, A. Liang *et al.*, Polarization-dependent selection rules and optical spectrum atlas of twisted bilayer graphene quantum dots, Phys. Rev. X **12**, 021055 (2022).

[15] Z. Y. Liu, S. Qiao, B. Huang, Q.-Y. Tang, Z.-H. Ling, W.-H. Zhang, H.-N. Xia, X. Liao, H. Shi, W. H. Mao *et al.*, Charge transfer gap tuning via structural distortion in monolayer $1T$-$NbSe_2$, Nano Lett. **21**, 7005 (2021).

[16] W. Ruan, Y. Chen, S. Tang, J. Hwang, H.-Z. Tsai, R. L. Lee, M. Wu, H. Ryu, S. Kahn, F. Liou *et al.*, Evidence for quantum spin liquid behaviour in single-layer $1T$-$TaSe_2$ from scanning tunnelling microscopy, Nat. Phys. **17**, 1154 (2021).

[17] Y. Geng, L. Lei, H. Dong, J. Guo, S. Mi, Y. Li, L. Huang, F. Pang, R. Xu, W. Zhou *et al.*, Hysteretic electronic phase transitions in correlated charge density wave state of $1T$-TaS_2, Phys. Rev. B **107**, 195401 (2023).

[18] M. H. Fischer, F. Loder, and M. Sigrist, Superconductivity and local noncentrosymmetricity in crystal lattices, Phys. Rev. B **84**, 184533 (2011).

[19] H. Y. Dong, P. H. Sun, L. Lei, Y. Y. Geng, J. F. Guo, Y. Li, L. Huang, R. Xu, F. Pang, W. Ji *et al.*, Emergent electronic kagome lattice in correlated charge-density-wave state of $1T$-TaS_2, arXiv:2301.05885.

[20] C. J. Butler, M. Yoshida, T. Hanaguri, and Y. Iwasa, Mottness versus unit-cell doubling as the driver of the insulating state in $1T$-TaS_2, Nat. Commun. **11**, 2477 (2020).

[21] S. H. Lee, J. S. Goh, and D. Cho, Origin of the insulating phase and first-order metal-insulator transition in $1T$-TaS_2, Phys. Rev. Lett. **122**, 106404 (2019).

[22] Y. D. Wang, W. L. Yao, Z. M. Xin, T. T. Han, Z. G. Wang, L. Chen, C. Cai, Y. Li, and Y. Zhang, Band insulator to Mott insulator transition in $1T$-TaS_2, Nat. Commun. **11**, 4215 (2020).

[23] J. J. Gao, J. G. Si, X. Luo, J. Yan, Z. Z. Jiang, W. Wang, Y. Y. Han, P. Tong, W. H. Song, X. B. Zhu *et al.*, Origin of the large magnetoresistance in the candidate chiral superconductor $4H_b$-TaS_2, Phys. Rev. B **102**, 075138 (2020).

[24] A. Achari, J. Bekaert, V. Sreepal, A. Orekhov, P. Kumaravadivel, M. Kim, N. Gauquelin, P. B. Pillai, J. Verbeeck, F. M. Peeters *et al.*, Alternating superconducting and charge density wave monolayerswithin bulk $6R$-TaS_2, Nano Lett. **22**, 6268 (2022).

[25] Y. Liu, W. J. Lu, L. J. Li, X. D. Zhu, W. H. Song, R. Ang, L. S. Ling, X. Z. Liu, and Y. P. Sun, Tuning the charge density wave and superconductivity in $6R$-$TaS_{2-x}Se_x$, Appl. Phys. **117**, 163912 (2015).

[26] A. Ribak, R. M. Skiff, M. Mograbi, P. K. Rout, M. H. Fischer, J. Ruhman, K. Chashka, Y. Dagan, and A. Kanigel, Chiral superconductivity in the alternate stacking compound $4H_b$-TaS_2, Sci. Adv. **6**, eaax9480 (2020).

[27] I. Silber, S. Mathimalar, I. Mangel, A. K. Nayak, O. Green, N. Avraham, H. Beidenkopf, I. Feldman, A. Kanigel, A. Klein *et al.*, Two-component nematic superconductivity in $4H_b$-TaS_2, Nat. Commun. **15**, 824 (2024).

[28] A. K. Nayak, A. Steinbok, Y. Roet, J. Koo, G. Margalit, I. Feldman, A. Almoalem, A. Kanigel, G. A. Fiete, B. H. Yan *et al.*, Evidence of topological boundary modes with topological nodal-point superconductivity, Nat. Phys. **17**, 1413 (2021).

[29] C. H. Wen, J. J. Gao, Y. Xie, Q. Zhang, P. F. Kong, J. H. Wang, Y. L. Jiang, X. Luo, J. Li, W. J. Lu *et al.*, Roles of the narrow electronic band near the Fermi level in $1T$-TaS_2−related layered materials, Phys. Rev. Lett. **126**, 256402 (2021).

[30] V. Vaňo, M. Amini, S. C. Ganguli, G. Chen, J. L. Lado, S. Kezilebieke, and P. Liljeroth, Artificial heavy fermions in a van der Waals heterostructure, Nature (London) **599**, 582 (2021).

[31] A. K. Nayak, A. Steinbok, Y. Roet, J. Koo, I. Feldman, A. Almoalem, A. Kanigel, B. Yan, A. Rosch, N. Avraham *et al.*, First order quantum phase transition in the hybrid metal-mott insulator transition metal dichalcogenide $4H_b$-TaS_2, Proc. Natl Acad. Sci. USA **43**, 120 (2023).

[32] Y. Liu, L. J. Li, W. J. Lu, R. Ang, X. Z. Liu, and Y. P. Sun, Coexistence of superconductivity and commensurate charge density wave in $4H_b$-$TaS_{2-x}Se_x$ single crystals, J. Appl. Phys. **115**, 043915 (2014).

[33] J. Bang, B. Lee, H. Yang, S. Kim, D. Wulferding, and D. Cho, Charge-ordered phases in the hole-doped triangular Mott insulator $4H_b$-TaS_2, Phys. Rev. B **109**, 195170 (2024).

[34] Z. K. Xie, M. Yang, Z. G. Cheng, T. P. Ying, J. G. Guo, and X. L. Chen, A revisit of superconductivity in $4H_b$-$TaS_{2-2x}Se_{2x}$ single crystals, J. Phys. Soc. Jpn. **92**, 054702 (2023).

[35] L. Crippa, H. Bae, P. Wunderlich, I. I. Mazi, B. H. Yan, G. Sangiovanni, T. Wehling, and R. Valentí, Heavy fermions vs doped Mott physics in heterogeneous Ta-dichalcogenide bilayers, Nat. Commun. **15**, 1357 (2024).

[36] See Supplemental Material at http://link.aps.org/supplemental/10.1103/PhysRevB.110.115107 for more details about STM, STS, and SKPM date.

[37] T. Shimada, F. S. Ohuchi, and B. A. Parkinson, Work function and photothreshold of layered metal dichalcogenides, Jpn. J. Appl. Phys. **33**, 2696 (1994).

[38] R. Ang, Z. C. Wang, C. L. Chen, J. Tang, N. Liu, Y. Liu, W. J. Lu, Y. P. Sun, T. Mori, and Y. Ikuhara, Atomistic origin of an ordered superstructure induced superconductivity in layered chalcogenides, Nat. Commun. **6**, 6091 (2015).

[39] C. Patra, T. Agarwal, R. R. Chaudhari, and R. P. Singh, Two-dimensional multigap superconductivity in bulk $2H$-TaSeS, Phys. Rev. B **106**, 134515 (2022).

[40] L. Ma, C. Ye, Y. Yu, X. F. Lu, X. H. Niu, S. Kim, D. Feng, D. Tománek, Y.-W. Son, X. H. Chen *et al.*, A metallic mosaic phase and the origin of Mott-insulating state in $1T$-TaS_2, Nat. Commun. **7**, 10956 (2016).

[41] S. Qiao, X. Li, N. Wang, W. Ruan, C. Ye, P. Cai, Z. Hao, H. Yao, X. Chen, J. Wu *et al.*, Mottness collapse in $1T$-$TaS_{2-x}Se_x$ transition-metal dichalcogenide: an interplay between localized and itinerant orbitals, Phys. Rev. X **7**, 041054 (2017).

[42] H. Y. Dong, Y. Y. Geng, J. F. Guo, L. Lei, Y. Li, L. Huang, F. Pang, R. Xu, W. Q. Yu, W. Ji *et al.*, Real-space hole-doping titration and manipulation of correlated charge density wave state in $1T$-TaS_2, arXiv:2401.01507.

[43] Q. X. Liu, P. H. Sun, F. Y. Meng, Y. Y. Geng, Z. H. Liu, J. F. Zhang, J. J. Gao, Z. C. Jiang, S. J. Tian, X. Luo *et al.*, Existence of an ultraflat band in the charge density wave state of $4H_b$-$TaS_{1.3}Se_{0.7}$, Phys. Rev. B **108**, 115115 (2023).

[44] X. Huang, T. M. Wang, S. N. Miao, C. Wang, Z. P. Li, Z. Lian, T. Taniguchi, K. Watanabe, S. Okamoto, D. Xiao *et al.*, Correlated insulating states at fractional fillings of the WS_2/WSe_2 moiré lattice, Nat. Phys. **17**, 715 (2021).

[45] J. M. Park, Y. Cao, K. J. Watanabe, T. Taniguchi, and P. J. Herrero, Tunable strongly coupled superconductivity in magic-angle twisted trilayer graphene, Nature (London) **590**, 249 (2021).

[46] S. H. Sung, N. Schnitzer, S. Novakov, I. E. Baggari, X. P. Luo, J. Gim, N. M. Vu, Z. D. Li, T. H. Brintlinger, Y. Liu *et al.*, Two-dimensional charge order stabilized in clean polytype heterostructures, Nat. Commun. **13**, 413 (2022).